The Astrophysical Journal, 776:75 (15pp), 2013 October 20 doi:10.1088/0004-637X/776/2/75

SEARCHING FOR NEUTRAL HYDROGEN HALOS AROUND $z \sim 2.1$ AND $z \sim 3.1$ Lyα EMITTING GALAXIES

John J. Feldmeier[1,11], Alex Hagen[2,3], Robin Ciardullo[2,3,11], Caryl Gronwall[2,3], Eric Gawiser[4,11], Lucia Guaita[5,11], Lea M. Z. Hagen[2,3], Nicholas A. Bond[6], Viviana Acquaviva[7], Guillermo A. Blanc[8], Alvaro Orsi[9,10], and Peter Kurczynski[4]

[1] Department of Physics and Astronomy, Youngstown State University, Youngstown, OH 44555, USA; jjfeldmeier@ysu.edu
[2] Department of Astronomy & Astrophysics, The Pennsylvania State University, University Park, PA 16802, USA
[3] Institute for Gravitation and the Cosmos, The Pennsylvania State University, University Park, PA 16802, USA
[4] Department of Physics and Astronomy, Rutgers, The State University of New Jersey, Piscataway, NJ 08854, USA
[5] Oskar Klein Cosmology Centre, Department of Astronomy, Stockholm University, SE-106 91 Stolkholm, Sweden
[6] Cosmology Laboratory (Code 665), NASA Goddard Space Flight Center, Greenbelt, MD 20771, USA
[7] Department of Physics, New York City College of Technology, City University of New York, 300 Jay Street, Brooklyn, NY 11201, USA
[8] Observatories of the Carnegie Institution of Washington, 813 Santa Barbara Street, Pasadena, CA 91101, USA
[9] Departamento de Astronomía y Astrofísica, Pontificia Universidad Católica, Av. Vicuña Mackenna 4860, Santiago, Chile
[10] Centro de Astro-Ingeniería, Pontificia Universidad Católica, Av. Vicuña Mackenna 4860, Santiago, Chile
Received 2012 December 21; accepted 2013 August 8; published 2013 September 30

ABSTRACT

We search for evidence of diffuse Lyα emission from extended neutral hydrogen surrounding Lyα emitting galaxies (LAEs) using deep narrow-band images of the Extended Chandra Deep Field South. By stacking the profiles of 187 LAEs at $z = 2.06$, 241 LAEs at $z = 3.10$, and 179 LAEs at $z = 3.12$, and carefully performing low-surface brightness photometry, we obtain mean surface brightness maps that reach 9.9, 8.7, and 6.2×10^{-19} erg cm^{-2} s^{-1} arcsec^{-2} in the emission line. We undertake a thorough investigation of systematic uncertainties in our surface brightness measurements and find that our limits are 5–10 times larger than would be expected from Poisson background fluctuations; these uncertainties are often underestimated in the literature. At $z \sim 3.1$, we find evidence for extended halos with small-scale lengths of 5–8 kpc in some but not all of our sub-samples. We demonstrate that sub-samples of LAEs with low equivalent widths and brighter continuum magnitudes are more likely to possess such halos. At $z \sim 2.1$, we find no evidence of extended Lyα emission down to our detection limits. Through Monte-Carlo simulations, we also show that we would have detected large diffuse LAE halos if they were present in our data sets. We compare these findings to other measurements in the literature and discuss possible instrumental and astrophysical reasons for the discrepancies.

Key words: cosmology: observations – galaxies: evolution – galaxies: halos – galaxies: high-redshift – galaxies: structure

Online-only material: color figures

1. INTRODUCTION

The star formation rates (SFRs) of high- and intermediate-redshift galaxies depend on the complex interplay between accretion and outflow. While infalling gas from the cosmic web provides fuel for starbursts (e.g., Dekel et al. 2009), the winds of young stars, supernovae, and active galactic nuclei (AGNs) cause feedback and dampen the intensity of the accretion (see Veilleux et al. 2005). The star formation history of a galaxy and its surrounding circumgalactic medium (CGM) are thus inextricably intertwined, and any model which seeks to reproduce the observed properties of these systems must take into account both of these processes (e.g., Davé et al. 2011b, 2011a).

Observationally, there is strong evidence for the presence of galactic-scale outflows around luminous star-forming galaxies at high redshift. At $z \sim 3$, the velocity offsets between resonance and non-resonance absorption features of Lyman-break galaxies (LBGs; e.g., Steidel et al. 1996, 2010; Adelberger et al. 2003; Shapley et al. 2003) and the relative strengths and velocities of multiple-peaked profiles of Lyα in emission (e.g., Verhamme et al. 2006, 2008; Tapken et al. 2007; Laursen et al. 2009; Barnes et al. 2011; Kulas et al. 2012) all point to outflows being common in these high luminosity systems. Outflows are also common in lower-luminosity objects: the spectral analyses of McLinden et al. (2011) and Berry et al. (2012) and, more recently, Hashimoto et al. (2013) clearly demonstrate that Lyα emitting galaxies (LAEs) at $z \sim 2$–3 have strong galactic winds. However, while the evidence for outflows is compelling, there is as of yet no direct evidence for the cold gas infall that is predicted by galaxy formation models (Steidel et al. 2010).

Detecting the circumgalactic material around high-redshift galaxies is a difficult proposition. Steidel et al. (2010) was able to infer the existence of this component out to ∼120 kpc by using angular pairs of unassociated $z \sim 2$–3 star-forming galaxies and looking for Lyα and Lyβ in absorption. However, a more direct approach is to search for circumgalactic material in emission. Resonant scattering can cause the Lyα photons produced inside a galaxy to scatter hundreds or even thousands of times before escaping into intergalactic space. Consequently, if a galaxy is surrounded by neutral hydrogen gas, that material is likely to be illuminated by Lyα. In fact, models by Zheng et al. (2011) suggest that at $z = 5.7$, diffuse Lyα emission in the CGM may be observable several hundred kiloparsecs from the site of its creation. In addition to inflows and outflows, a clumpy and inhomogeneous interstellar medium (ISM) may also create halo-like structures (e.g., Verhamme et al. 2012).

[11] Visiting astronomer, Cerro Tololo Inter-American Observatory, National Optical Astronomy Observatory, which are operated by the Association of Universities for Research in Astronomy, under contract with the National Science Foundation.

The recent observations by Steidel et al. (2011, hereafter S11) appear to confirm this prediction. By co-adding Keck, Hale, and Subaru narrow-band images of 92 LBGs between $2.2 < z < 3.2$, S11 claimed the detection of scattered Lyα from a diffuse halo that extends ~80 kpc from their mean composite galaxy. The azimuthally averaged surface brightness profile of this halo is exponential, with a scale length that is substantially larger than that of the galaxy's continuum but similar to that measured for Lyα blobs (e.g., Steidel et al. 2000; Matsuda et al. 2004; Saito et al. 2006; Prescott et al. 2012). This consistency led S11 to argue that Lyα halos are a generic feature of all high-redshift star-forming galaxies, and that these halos have self-similar exponential profiles.

However, the galaxies targeted by S11 were all selected via the Lyman-break technique, and are thus among the brightest and most massive galaxies in the high-redshift universe. With stellar masses of $\sim 2 \times 10^{10}\ M_{\odot}$, SFRs of $\sim 30\ M_{\odot}\ \mathrm{yr}^{-1}$, and internal extinctions of $A_V \sim 1$ (e.g., Shapley et al. 2001; Adelberger et al. 2005; Stark et al. 2009; Finkelstein et al. 2010; Labbé et al. 2010) these objects are in the extreme. Most high-z-objects have much lower masses and SFRs, and are not detectable via the Lyman-break technique. To test the ubiquity of Lyα halos, more representative samples of objects are needed.

LAEs may be a better population for this purpose. Thousands of LAE candidates have been detected over a very large range of redshifts using a variety of observational techniques, and their properties have been intensely studied (e.g., Ouchi et al. 2008, 2010; Rauch et al. 2008; Finkelstein et al. 2009a; Wang et al. 2009; Östlin et al. 2009; Nilsson et al. 2009, 2011; Hu et al. 2010; Ono et al. 2010; Ota et al. 2010; Hibon et al. 2010; Tilvi et al. 2010; Guaita et al. 2010; Cassata et al. 2011; Cowie et al. 2011; Adams et al. 2011; Ciardullo et al. 2012; Barger et al. 2012; Oteo et al. 2012; Mallery et al. 2012; Nakajima et al. 2012; Krug et al. 2012 and references within). Although LAEs can have Lyα luminosities similar to that of LBGs, most have SFRs (SFR $\sim 2\ M_{\odot}\ \mathrm{yr}^{-1}$) and stellar masses ($M \lesssim 10^9\ M_{\odot}$) that are an order of magnitude less (e.g., Gawiser et al. 2006a; Pirzkal et al. 2007; Lai et al. 2008; Finkelstein et al. 2009b; Ono et al. 2010; Yuma et al. 2010). These are the objects that will likely evolve into present-day L^* galaxies like the Milky Way (e.g., Pirzkal et al. 2007; Gawiser et al. 2007; Guaita et al. 2010; Salvadori et al. 2010; Yajima et al. 2012).

An additional advantage of LAEs is that they are relatively metal-poor and dust-poor, with most having internal extinctions $A_V \lesssim 0.5$ (e.g., Nilsson et al. 2007; Gawiser et al. 2007; Ono et al. 2010; Acquaviva et al. 2011; Finkelstein et al. 2011c, 2011a; Blanc et al. 2011; however, also see Finkelstein et al. 2009b and Nakajima et al. 2012 for contrasting views). This lack of dust makes it more likely that the Lyα photons generated in the systems' star-forming regions will escape, although strong outflows in LBGs may also produce similar escape fractions. Finally, spectroscopy has shown that the contamination rate of photometrically selected LAEs at $z < 3.1$ is small, less than 2% (Gronwall et al. 2007; Ouchi et al. 2008; Berry et al. 2012). Thus, large samples of Lyα emitters are relatively straightforward to obtain.

Recently, Matsuda et al. (2012, hereafter M12) used the co-added images of ~2100 LAEs to conclude that the properties of Lyα halos depend on environment, with the emission surrounding LAEs in low density environments being much fainter than that for corresponding objects in overdense regions. However, neither S11 nor M12 explored the systematic effects which limit the depth to which image stacking can be trusted. Invariably, the true limit of any surface brightness analysis is significantly brighter than that which is inferred from simple counting statistics.

The S11 study focused on cluster LBGs at $2.3 < z < 3.1$ while M12 focused on LAEs at $z \sim 3.1$ in a range of galaxy environments. In this paper, we investigate the extended Lyα halos of field LAEs at similar redshifts. In Section 2, we define our samples using the $z \sim 3.1$ observations of Gronwall et al. (2007) and Ciardullo et al. (2012), and the $z \sim 2.1$ data of Guaita et al. (2010). In Section 3, we describe our stacking technique and present the initial analysis of the Lyα profiles of our LAE sub-samples. Then in Section 4, we perform a detailed analysis of the various effects that limit the precision of stacking analyses, and show that the systematic uncertainties in this procedure have generally been underestimated. In Section 5, we present a more detailed stacking analysis, and demonstrate that there is evidence for extended Lyα-emission in some, but not all of our samples, down to surface brightnesses of $\approx 8 \times 10^{-19}$ erg cm^{-2} s^{-1} arcsec^{-2} at $z \sim 3$ and $\approx 1 \times 10^{-18}$ erg cm^{-2} s^{-1} arcsec^{-2} at $z \sim 2$. We show that stacks containing sources that have relatively low Lyα equivalent widths and/or bright continuum magnitudes are more likely to show extended Lyα emission than similar stacks with low continuum luminosities or high equivalent widths. In Section 6, we compare our results to previous studies via a series of Monte-Carlo simulations and demonstrate that halos such as those found by S11 would have been easily detected in our survey. In Section 7, we discuss possible explanations for our results, including the extended telescope point-spread function (PSF), the limitations of sky subtraction, the intrinsic differences between galaxy populations, the effects of environment and orientation, and the possible evolution of Lyα halos between $z \sim 3$ and $z \sim 2$. Finally, in Section 8, we summarize our results and discuss the possible ways of improving the constraints on Lyα halos with upcoming surveys and new Lyα radiative transfer models.

For this paper, we assume a ΛCDM cosmology with $\Omega_\lambda = 0.70$, $\Omega_m = 0.3$, and $H_0 = 70$ km s^{-1} Mpc^{-1}. With these values, $1'' = 8.32$ kpc at $z = 2.1$ and 7.63 kpc at $z = 3.1$.

2. THE SAMPLE OF Lyα EMITTERS

In order to test for the existence of diffuse emission around LAEs, we consider three statistically complete sets of these objects. Each set is located in the Extended Chandra Deep Field South (ECDF-S; Lehmer et al. 2005), each was identified via narrow-band imaging with the Mosaic II CCD camera (Muller et al. 1998) on the CTIO Blanco 4 m telescope, and each defines an LAE as an emission-line galaxy with a rest-frame Lyα equivalent width greater than 20 Å. The statistically complete sample of LAEs in each data set was defined by finding all LAEs with fluxes greater than the 90% completeness level, where the completeness curve was determined from artificial star simulations.

Our first set of LAEs is that found by Gronwall et al. (2007) using a 50 Å FWHM filter centered at 4990 Å. This dataset, hereafter called C-O3, covers the redshift range $3.08 < z < 3.12$ and is 90% complete to a monochromatic Lyα emission-line luminosity limit of $\log L = 42.1$ erg s^{-1}. A total of 254 objects were identified in this survey, though only 156 are members of the statistically complete sample. To date, 67 of these LAEs have been spectroscopically confirmed as $z \sim 3.1$ star-forming galaxies (the first 61 confirmations are reported in Gawiser et al. 2007). The median seeing for this survey was 1.″0.

The second set of LAEs is that found by Ciardullo et al. (2012), using a 57 Å FWHM filter centered at 5010 Å. This LAE catalog, hereafter called K-O3, is 90% complete to $\log L > 42.3$ erg s^{-1}, and has considerable overlap with that of Gronwall et al. (2007). However, because the K-O3 central wavelength is slightly redder than that of C-O3, the dataset also contains 68 new objects in the redshift range $3.10 < z < 3.15$. This K-O3 survey discovered 199 LAE candidates; 130 of these are in the statistically complete sample. The median seeing for this survey was 1.″1.

Our third sample of LAEs examines a different redshift regime. By using a 50 Å FWHM filter centered at 3727 Å, Guaita et al. (2010) were able to identify 250 LAE candidates in the redshift range $2.04 < z < 2.09$. Guaita et al. (2011) further refined this sample, by improving the photometry, removing one probable AGN, and using *Hubble Space Telescope* (*HST*) morphological measurements to exclude 34 likely interlopers. This left a final sample consisting of 201 objects, of which 73 are brighter than a 90% completeness limit of $\log L = 41.8$ erg s^{-1}. We define this as the O2 LAE sample. The median seeing for this survey was 1.″4.

Since all three surveys targeted a region of space with deep *Chandra* data, most quasars and other AGNs have been eliminated from the samples based on their X-ray emission (Lehmer et al. 2005; Virani et al. 2006; Luo et al. 2008). Similarly, because the ECDF-S has been subjected to deep near-UV (1700–2800 Å) surveys by the *GALEX* and *Swift* satellites (Schiminovich et al. 2003; Hoversten et al. 2009), most foreground interlopers have already been identified. (For the redshifts under consideration, the rest-frame near-UV lies blueward of the Lyman break.) Thus, our samples of LAEs should be relatively clean. Of the 73 $z \sim 3.1$ LAEs with spectroscopic confirmations, *all* have redshifts that place the galaxy between $3.08 < z < 3.12$. Similarly, of the 13 $z = 2.1$ objects with spectroscopic redshifts (Berry et al. 2012), there are no foreground contaminants.

Finally, we should note that almost 300 LAEs in the E-CDFS (171 at $z \sim 3.1$ and 108 at $z \sim 2.1$) have been imaged in the rest-frame ultraviolet with *HST*'s Advanced Camera for Surveys. An analysis of these data by Bond et al. (2012) has shown that in V_{606}, LAEs in the redshift range $2 < z < 3$ are extremely compact, with median half-light radii less than 0.″2. In fact, at $z = 3.1$, the largest half-light radius recorded is 0.″29 and the largest half-light radius at $z = 2.1$ is 0.″43. In both cases, this is much smaller than the seeing of the ground-based images under consideration (1.″0 and 1.″4), respectively. Similar results have been found for other LAE samples over a wide range of redshift (e.g., Malhotra et al. 2012 and references within). Consequently, if the Lyα emission emanating from these objects has the same spatial distribution as the UV light, the profiles of these objects should be consistent with those of the frames' PSFs.

3. INITIAL STACKING OF Lyα EMITTERS

To search for extended Lyα emission, we began with the stacked Mosaic II images obtained by Gronwall et al. (2007), Guaita et al. (2010), and Ciardullo et al. (2012). First, a small $27'' \times 27''$ (101×101 pixel) region was extracted about the center of each LAE. To avoid edge effects, any source close to the CCD boundaries was excluded at this step. This left us with 146, 124, and 69 sources in the statistically complete C-O3, K-O3, and O2 samples, and 241, 179, and 187 objects in the total samples of these surveys, respectively. Next, to examine the behavior of Lyα halos in our highest mass objects, we used the broadband magnitudes of the MUSYC survey (Gawiser et al. 2006b) to define sub-samples of LAEs more luminous than $R_{AB} = 25.5$. With this limit, these LAE sub-samples have photometric and spectroscopic properties similar to those of the "LAE only" sample of LBGs studied by S11. These sub-samples, which we will refer to as "UV bright," contain 28, 19, and 27 sources in the C-O3, K-O3, and O2 samples, respectively.

Finally, to examine whether equivalent width has any affect on the properties of Lyα halos, we ranked our LAEs by their (photometrically derived) rest-frame equivalent widths, and created sub-samples of objects in the highest and lowest quartiles of the distribution. We refer to these sub-samples as "high EW" and "low EW," and each contains 60, 44, and 50 objects in the C-O3, K-O3 and O2 datasets, respectively. For the low-EW sub-samples, the rest-frame equivalent widths range from 20 Å to 60 Å; for the high-EW sub-set, $EW_0 > 74$ Å, with most of the objects having rest-frame equivalent widths greater than 100 Å. We note that since the distribution of LAE equivalent widths has (at best) a weak dependence on galaxy luminosity (Gronwall et al. 2007; Ciardullo et al. 2012), samples chosen by equivalent width and UV-brightness are somewhat orthogonal. For example, in the C-O3 data, only ~25% of the low-equivalent width LAEs (16 out of 60) are members of the UV-bright sample; for the K-O3 sample, this fraction is ~35% (16 out of 44), and for O2, the fraction is ~44% (22 out of 50). A summary of the different sub-samples, and other relevant information, is given in Table 1.

After defining the LAE sub-samples, the next step involved co-adding the individual LAE images to create a high signal-to-noise stacked image. We did this by scaling each object to a common narrow-band flux level and then combining the images, using the imcombine task within IRAF[12], and adopting a (3σ) sigma-clipping algorithm with a scheme which weighted each source by its total flux. This procedure is different than the stacking procedure of S11, who used straight averages with masking for their stacks, and is slightly different than M12, who used a median combination but did not scale or weight their sources. To avoid any effects of interpolation, we used only integer pixel shifts for each stack; this procedure has the effect of slightly increasing the radial surface brightness profile. The stacking procedure was used both on the original narrow-band images themselves, and on continuum-subtracted images, where the flux level at 5000 Å was defined using the *B* and *V* frames of the MUSYC survey (Gawiser et al. 2006b). For the O2 data, the continuum flux at 3727 Å was derived from publicly available *U* and *B* frames taken with the Wide Field Imager (WFI) of the ESO 2.2 m telescope (Hildebrandt et al. 2006) that were reprojected to match the MUSYC *BVR* image of the same field. These continuum subtracted images have the advantage of decreasing the contamination from nearby continuum sources, but come with the penalty of decreased signal-to-noise and possible mismatches in the frames' PSFs.

Finally, as a control on our experiments, we also analyzed a catalog of point sources initially found by Altmann et al. (2006) on the MUSYC broad-band images. This catalog, which consists of objects with the colors of Galactic K- and M-type stars, was further refined by Bond et al. (2011) using *HST*/WFC3 Early Release Science images (ERS; Windhorst

[12] IRAF is distributed by the National Optical Astronomy Observatory, which is operated by the Association of Universities for Research in Astronomy (AURA) under cooperative agreement with the National Science Foundation.

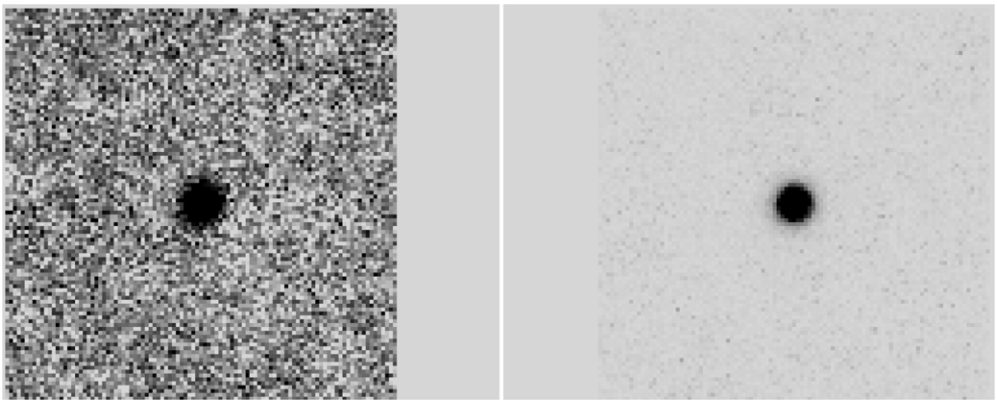

Figure 1. On the left is the median-combined statistically complete sub-sample of 146 C-O3 Lyα emitters; on the right is the median-combined sample of 55 stellar sources from the same image. The grayscale stretch is linear for each stack, and ranges from -1σ to 0.15p, where σ is the standard deviation of the pixels near the corners of each image and p is the peak pixel value in ADU. There is no apparent difference between the two stacks. Formally, the FWHM of the Lyα emitters is 8% larger than the stellar sources, but the uncertainties are of comparable magnitude (5%).

Table 1
Sub-sample Properties

Sample	Number of LAEs	$\langle z \rangle$	Median Seeing	Effective Narrow-band Exposure Time (hr)	EW[a] Range (Å)	EW[a] Median (Å)
C-O3 total	241	3.10	1.″0	24.00	20–366	54
C-O3 statistically complete	146	3.10	1.″0	24.00	20–366	51
C-O3 UV bright	28	3.10	1.″0	24.00	20–158	30
C-O3 high EW	60	3.10	1.″0	24.00	82–366	103
C-O3 low EW	60	3.10	1.″0	24.00	20–36	27
K-O3 total	179	3.12	1.″1	15.67	20–628	63
K-O3 statistically complete	124	3.12	1.″1	15.67	20–628	60
K-O3 UV bright	19	3.12	1.″1	15.67	22–49	23
K-O3 high EW	44	3.12	1.″1	15.67	94–628	125
K-O3 low EW	44	3.12	1.″1	15.67	20–40	29
O2 total	187	2.07	1.″4	35.75	20–933	43
O2 statistically complete	69	2.07	1.″4	35.75	27–933	70
O2 UV bright	27	2.07	1.″4	35.75	20–60	26
O2 high EW	46	2.07	1.″4	35.75	74–933	98
O2 low EW	46	2.07	1.″4	35.75	20–28	23

Note. [a] Equivalent widths are all rest-frame, and were determined from photometry.

et al. 2011) of the GOODS-S region. These objects were re-identified on our narrow-band frames, and stacked in a manner identical to that for the LAEs. Fifty-five stars formed the point-source stack on our C-O3 and K-O3 images; for the O2 data, our control image was created using the median of nineteen stars.

Figure 1 compares the median-stacked image of the 146 $z = 3.1$ LAEs in the statistically complete C-O3 sub-sample to that of the field's point sources. A careful examination of the figure reveals no compelling evidence for extended Lyα emission. The results for the other stacks are similar: there is no clear signature of extended Lyα emission in any of the LAE sub-samples. Table 2 quantifies this result by listing the FWHM of a two-dimensional Gaussian fit to each image stack, as measured with the `fitpsf` task within IRAF. The uncertainties on the fits for each stack are derived from a bootstrap analysis, in which we randomly resampled the sources (with replacement) and repeated the `imcombine` and `fitpsf` steps 30 times for each stack. For comparison, the FWHM of the point-source stacks are also shown, and the LAE measurements are tabulated with respect to these values. As the table demonstrates, there is a suggestion that some of the LAE stacks have broader radial profiles than that of the PSF stars. However, the uncertainties in this type of analysis are large and no obvious trends are apparent between the different sub-samples. Moreover, this simple procedure does not fully account for the effects of centroiding errors: because the LAEs are much fainter than the comparison stars, the FWHM of their stacks are expected to be wider due to positional uncertainties. A more sophisticated analysis is therefore needed to find evidence of Lyα halos.

4. SURFACE BRIGHTNESS LIMITATIONS

Before proceeding further, we need to examine the realistic limits of our surface brightness measurements, and properly characterize any systematic uncertainties. This is not a straightforward process. Surface photometry at faint flux levels has additional uncertainties above and beyond those produced by Poisson statistics. Large-scale flat-fielding errors, the structure of the PSF at large radius, and errors in the estimation of the sky background all introduce systematic uncertainties into surface brightness measurements, and these errors dominate the error budget at low surface brightnesses. Such uncertainties are well known in the astronomical literature, (e.g., Morrison et al. 1994; Zheng et al. 1999; Gonzalez et al. 2005; Zibetti et al. 2005; Krick et al. 2006; Bernstein 2007) and countermeasures involving better telescope baffling (e.g., Grundahl & Sorensen 1996), advanced flat-fielding techniques (such as drift-scanning, or creating high quality dark-sky flats; e.g., Zheng et al. 1999;

Table 2
Results from Two-dimensional Gaussian Fitting

Sample	C-O3		K-O3		O2	
	FWHM (arcsec)	Ratio[a]	FWHM (arcsec)	Ratio[a]	FWHM (arcsec)	Ratio[a]
Stacked stars	1.23 ± 0.03	1	1.23 ± 0.04	1	1.40 ± 0.09	1
Total sample	1.39 ± 0.04	1.13 ± 0.04	1.28 ± 0.03	1.04 ± 0.04	1.53 ± 0.07	1.09 ± 0.09
Statistically complete	1.33 ± 0.05	1.08 ± 0.05	1.32 ± 0.02	1.07 ± 0.03	1.58 ± 0.07	1.13 ± 0.09
UV bright	1.36 ± 0.07	1.11 ± 0.06	1.25 ± 0.05	1.01 ± 0.05	1.54 ± 0.17	1.10 ± 0.14
High EW	1.19 ± 0.07	0.97 ± 0.06	1.19 ± 0.04	0.96 ± 0.04	1.48 ± 0.07	1.06 ± 0.08
Low EW	1.35 ± 0.09	1.10 ± 0.08	1.28 ± 0.05	1.04 ± 0.04	1.31 ± 0.08	0.94 ± 0.08
Difference total	1.28 ± 0.04	1.04 ± 0.04	1.21 ± 0.23	0.99 ± 0.19	1.09 ± 0.11	0.78 ± 0.09
Difference statistically complete	1.45 ± 0.08	1.18 ± 0.07	1.45 ± 0.18	1.18 ± 0.15	1.62 ± 0.15	1.16 ± 0.13

Note. [a] Defined as FWHM (sub-sample)/FWHM (stacked stars), with the uncertainties from each sample added in quadrature.

Gonzalez et al. 2005), and using optical systems that minimize internal reflections (Slater et al. 2009) have been developed. There has also been numerous efforts to develop more robust and precise algorithms for flat-fielding, sky subtraction, and the removal of foreground objects in ultra-deep surface photometry studies (e.g., Morrison et al. 1994; Melnick et al. 1999; Gonzalez et al. 2000; Krick et al. 2006; Martínez-Delgado et al. 2008; Paudel et al. 2013). Unfortunately, these techniques are not always applied in practice or are logistically difficult to implement. As a result, surface photometry on large telescopes with wide-field imagers will have a non-negligible amount of systematic uncertainty at low surface brightness. This applies to our own dataset, but it is very likely that other observations with similar systems will also have these effects.

The dominant systematic uncertainty for ultra-deep surface photometry is usually the large-scale flat-fielding error (Morrison et al. 1994; Feldmeier et al. 2004). In order to empirically determine this error on the C-O3, K-O3, and O2 survey data, we followed the procedures described in Feldmeier et al. (2002, 2004) and Rudick et al. (2010). In brief, we began by using DAOPHOT (Stetson 1987) to find and measure the magnitude of every point source on the frame. We then determined a more precise small-scale PSF for each image (out to the larger radius of $\sim 5''$), while masking out all of the point sources down to an estimated level of $0.1/t_{\rm exp}$ ADU, where $t_{\rm exp}$ is the exposure time and ADU is the number of counts above the sky value. We next identified a saturated star in each image, and, after masking all other nearby sources, used it to construct an azimuthally averaged PSF out to a much larger radius ($50''$–$60''$, depending on the image and the brightness of the chosen star). As was found originally by King (1971), the PSF of a ground-based telescope extends out to a very large radius, and has a dramatic change in slope in the far field. As displayed in Figure 2, once outside of $\sim 4''$ (i.e., $\sim$30 kpc at the redshift of our objects), the PSF contains flux far above that which would be predicted from a simple Gaussian extrapolation. Note the difference between the PSF of the O2 image and that of the two images near 5000 Å. This is due to the differing patterns of internal reflections between the CCD dewar window and the narrow-band filter (Slater et al. 2009). Measurements of the large-scale PSF by other authors (see the detailed discussion by Bernstein 2007) indicate that the shape of this function depends not only on the telescope, instrument, and wavelength, but on the observing season as well, as observations taken several months apart may have very different power-law slopes at large radii. Consequently, any analysis that relies on subtracting the large-scale PSFs of different telescopes and/or instruments must be treated with suspicion. To be conservative, the remainder of this paper will focus solely on our narrow-band data alone; no attempt will be made to interpret our continuum-subtracted images.

With the large-scale PSF determined, we re-masked all of the point sources in the frame, again down to a level of $0.1/t_{\rm exp}$ ADU. We then masked out all of the frame's non-point sources, using the SExtractor software package version 2.2.2 (Bertin & Arnouts 1996) and the procedures of Feldmeier et al. (2002, 2004). Finally, after careful inspection, we manually masked any remaining regions of flux (less than 1% of the remaining imaging area). An illustration of the different steps of our masking procedure can be found in Figure 9 of Feldmeier et al. (2002).

After applying this mask, we block-averaged the remaining pixels into 49×49 pixel ($13\farcs1 \times 13\farcs1$) superbins and calculated the robust mean of each superbin (Morrison et al. 1994), while excluding from the analysis all superbins containing less than 100 unmasked pixels. This latter condition is rarely important, as it is only used when a superbin contains an extremely bright star or a nearby galaxy. In our blank-field images, the median number of pixels within each superbin was 2125, 2010, and 1957 for the C-03, K-03, and O2 images, respectively. Given the large size of these superbins, each of their mean values should be equal to the sky subtracted mean of the image. However, as the histograms of Figure 3 illustrate, there is a significant amount of dispersion about the sky subtracted mean. This is the effect of large-scale flat-fielding errors, and the wings of stars and galaxies that remain unmasked despite our procedures.

We conservatively define the large-scale flat-fielding error as the FWHM of these distributions; these values are given in Column 2 of Table 3. As a cross-check of our analysis, we also determined the standard deviation of the sky background at the edges of our LAE and point-source image stacks. These values will not be identical to those derived from the superbins for two reasons: (1) the effect of scaling each individual image to a common flux level, and (2) the differing spatial distribution of the LAEs compared to the sky histograms. Nevertheless, the values obtained from the sky background of the stacked images are within 50% of the adopted values of Table 3.

The third and fourth columns of Table 3 compare the large-scale flat-fielding errors to the median sky values of the parent image. These uncertainties are comparable to those found for other deep imaging surveys (e.g., Feldmeier et al. 2004; Rudick et al. 2010), but are not as good as the those associated with the original MUSYC broad-band survey (see Table 5 of Gawiser et al. 2006b). We attribute this difference to the lower flux values associated with our narrow-band data: although the MUSYC

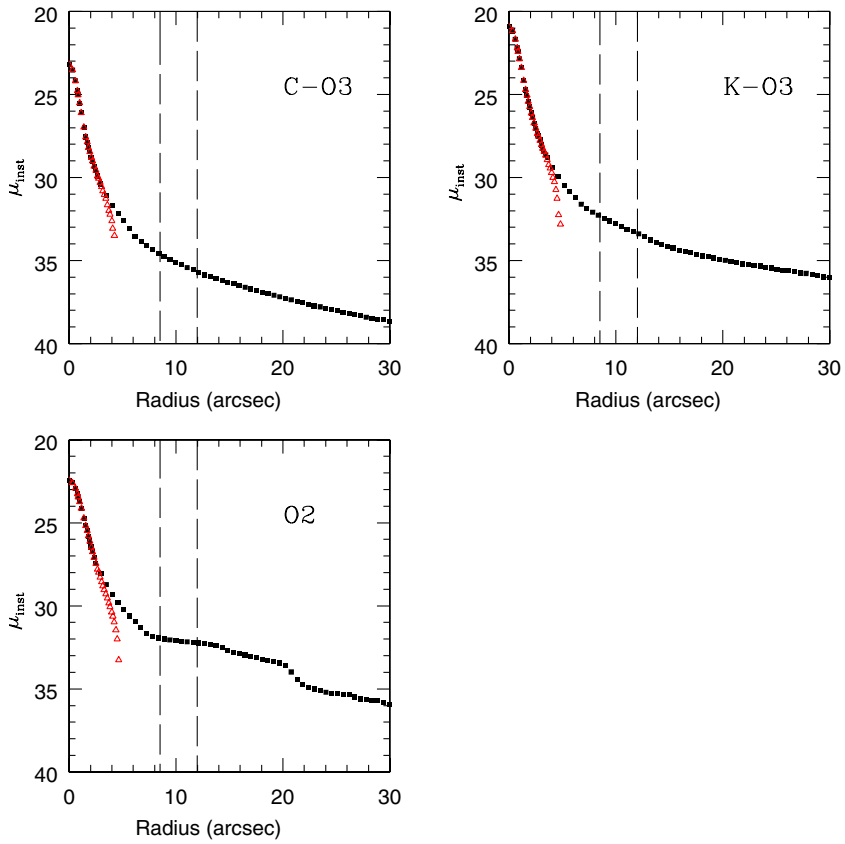

Figure 2. Azimuthally averaged surface brightness profile of a star constructed for each of our narrow-band images. The instrumental surface brightness scale, μ_{inst} is defined as 1 ADU $s^{-1} = 25$ mag $arcsec^{-2}$. The red open triangles denote the small-scale PSF, as measured by bright stars and the DAOPHOT software package. The filled squares represent the merger of the DAOPHOT PSF (at small radii) with the azimuthally averaged profile of a saturated star (at large radii), where the large-scale PSF was normalized to the small-scale PSF. For reference, the dashed vertical lines shows the radial extent studied by S11 (12″) and M12 (8.″5) in their analyses.
(A color version of this figure is available in the online journal.)

Table 3
Large-scale Flat-field Uncertainties

Field	Histogram FWHM[a] (10^{-4} ADU s^{-1} bin^{-1})	Median Sky Value (ADU s^{-1} $pixel^{-1}$)	Uncertainty[b] (%)	Exposure Time (s)	N[c]	Expected Poisson Error (10^{-4} ADU s^{-1} bin^{-1})	Flux Error[d]
C-O3	1.30	0.078	0.167	3600	24	0.122	8.7
K-O3	1.15	0.174	0.066	1200	47	0.224	6.2
O2	0.75	0.061	0.123	3600	36	0.088	9.9

Notes.
[a] See Figure 3 and the discussion in the text.
[b] Defined as Histogram FWHM/Median Sky Value.
[c] Effective number of exposures for each field.
[d] Final units are 10^{-19} erg s^{-1} cm^{-2} $arcsec^{-2}$.

images were taken with the same telescope and reduced using similar techniques, the increased count rate of the background sky depressed the relative importance of additive sky terms. By using the exposure times of each dataset (given in the fifth column), the effective number of exposures (given in the sixth column), and the typical Mosaic II CCD gain of 2.55 e^{-1} per ADU, a representative Poissonian error measured in ADU can be calculated for each superbin as follows:

$$\sqrt{\frac{S}{TgAN}} \quad (1)$$

where S is the median sky value given in units of ADU s^{-1} per pixel, T is the exposure time in seconds, g is the adopted gain of the CCDs, A is the area of each superbin in pixels, (we adopted 49×49 pixels in this case), and N is the effective number of exposures. These uncertainties are given in the seventh column of Table 3. Comparing the two uncertainties, we find that large-scale flat-fielding error is 5–10 times larger than the Poisson value. This noise floor cannot be reduced by simply including more sources in the stack, or binning the overall results: it is intrinsic to the data. The final column in Table 3 gives this fundamental limit in units of monochromatic surface brightness.

5. DETAILED STACKING

With the systematic uncertainties of our datasets better determined, we began a more detailed analysis of the surface brightness profiles of LAEs. To do this, we azimuthally

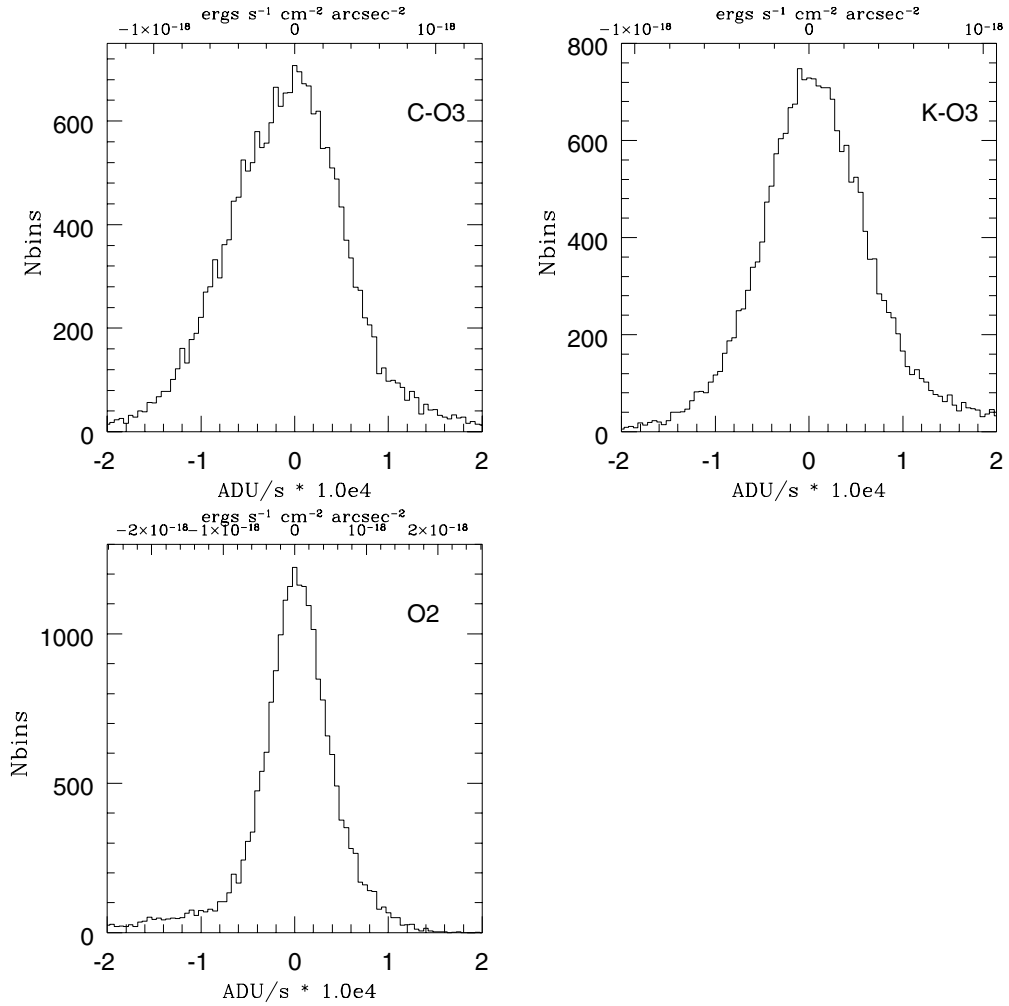

Figure 3. Histogram of sky values for each of our block-averaged images, binned into intervals of 5.0×10^{-6} ADU s^{-1} bin^{-1}. Ideally, the sky values should all equal zero. However, due to large-scale flat-fielding errors and the faint unmasked wings of stars and galaxies, there is usually a dispersion about zero in observed data. This distribution determines the limiting surface brightness of our analysis.

averaged each stacked narrow-band image using a harsh (2.5σ) sigma-clipping algorithm, thereby creating a series of radial bins extending 18.″7 (70 pixels) from the source center. Uncertainties for each radial bin were calculated using a full error model, including readout noise, photon noise, small-scale flat-fielding error, and large-scale flat-fielding error, and were determined in a similar manner as in Feldmeier et al. (2004; see their Appendix for a full description). Next, we determined a new local sky value for each stack, by computing the median pixel value in a circular annulus between 13.″4 and 18.″7 (50–70 pixels) from the LAE centroid. At $z \sim 2.1$, this annulus corresponds to a linear distance of between 111 and 156 kpc; at $z \sim 3.1$, the range is between 102 and 142 kpc. In all cases, the local sky was within ∼1% of the original sky value, and so the additional uncertainty introduced at this step was small (on average a factor of two less than the large-scale flat-fielding error). This constant sky value was then subtracted from the radial profiles.

The resulting sky-subtracted radial profiles are plotted in Figures 4–6. Also shown in these figures are the frames' total PSFs (core and large-scale; calculated in Section 4), the radial profiles derived from the stacked set of point sources, and the surface brightness limits defined by the frames' large-scale flat-fielding errors. In each figure, the comparison profiles have been scaled in flux to match the three innermost points (0.″–0.″6) of the corresponding LAE. We note that the lines representing the surface brightness limits are approximate, since they represent the mean flat-fielding error of the field. Since LAEs exhibit angular clustering (e.g., Francke 2009), the large-scale flat-fielding error appropriate to the stacked images may be slightly different. Nevertheless, they do illustrate the level at which stacks made from the wide-field Mosaic imager become suspect.

To better summarize the profiles displayed in Figures 4–6, we subtracted the point source profile from each LAE sub-sample stack, again using the three innermost points for scaling. Next, following S11 and M12, we fit the residuals to the exponential profile:

$$S(r) = C_n \exp(-r/r_n) \quad (2)$$

where C_n is the normalization factor, and r_n is the exponential scale length, using a Levenberg–Marquardt non-linear least-squares algorithm (Press et al. 1992), which took into account negative fluxes for sky-subtracted bins. The results of these fits are given in Table 4. The uncertainties given in the table are the internal errors from the fit themselves, and are likely to be underestimates to the true uncertainties. For practical reasons, our fits were restricted to the spatial scales between 0.″75 (where seeing effects dominate) to 8.″0, where large-scale flat-fielding

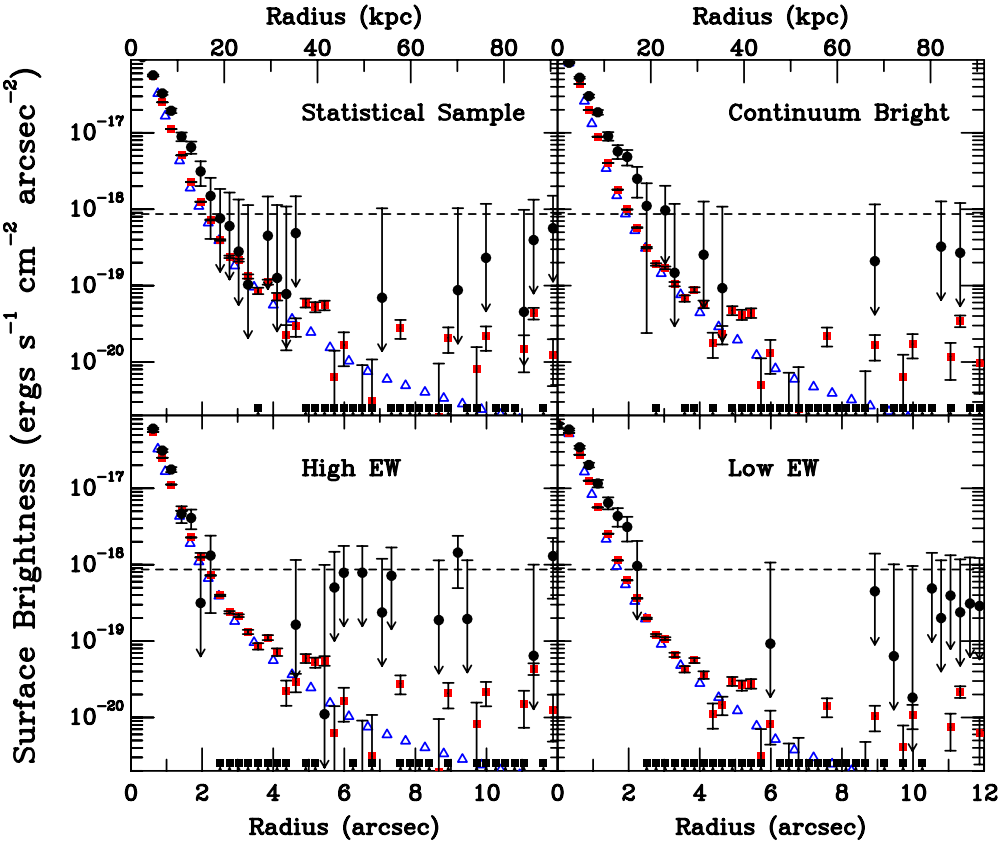

Figure 4. Radial profiles of the LAEs derived from the C-O3 sample. For each of these figures, the black circles represent the radial profile of the stacked LAEs, the blue open triangles represent the large-scale PSF, as determined in Section 4, and the red squares show the stacked radial profile of the stellar sources found in each frame. LAE bins that have negative flux are denoted by a filled point at the bottom of each plot. The large-scale PSF and stellar sources have been normalized to match the three innermost points of the LAE profile. The horizontal dashed line represents the flux limit comparable to our systematic uncertainties. The differing profiles relate to the statistically complete sub-sample (top left), the UV bright sub-sample (top right), the high-EW sub-sample (bottom left) and the low-EW sub-sample (bottom right), respectively.

(A color version of this figure is available in the online journal.)

Table 4
Point-source Subtracted Exponential Fits

	C-O3		K-O3		O2	
Sample	C_n[a]	r_n (kpc)	C_n[a]	r_n (kpc)	C_n[a]	r_n (kpc)
Statistically complete	3.6 ± 1.1	5.7 ± 1.0	3.1 ± 1.5	4.4 ± 1.0	1.3 ± 1.6	5.4 ± 3.7
UV bright	3.8 ± 1.0	6.0 ± 0.9	1.3 ± 0.6	6.4 ± 1.8	1.5 ± 1.5	5.7 ± 3.2
High EW	1.5 ± 1.2	5.5 ± 2.6	1.3 ± 6.8	2.8 ± 5.0	0.6 ± 0.4	3.7 ± 12
Low EW	2.4 ± 1.1	5.8 ± 1.5	1.2 ± 0.3	8.4 ± 1.5	0.4 ± 1.6	5.5 ± 11

Note. [a] Flux is in units of 10^{-17} erg cm^{-2} s^{-1} arcsec^{-2}.

errors begin to make all measurements consistent with zero. Moving the inner radius outward to match the 1.″0 value used by S11 does not qualitatively change the results.

An inspection of Figures 4–6 and Table 4 reveals several interesting patterns. At $z \sim 3$, there is evidence for the existence of extended Lyα halos in some of the LAE sub-samples. Specifically, the data suggest that UV continuum bright LAEs are slightly more extended than the general LAE population, and low-equivalent width objects have larger halos than their high-equivalent width counterparts. Since the effect is present on stacks made from both the C-O3 and K-O3 frames, this suggests that the effect is real, and that there is a genuine difference between LAEs with strong and weak Lyα emission. The sub-samples that show evidence for extended Lyα halos are plotted in Figure 7 in residual form, along with the best-fitting exponential profile. For comparison purposes, the "LAE only" exponential fit of S11 and the "$-1 < \delta^a_{\rm LAE} < 0.5$" exponential fit of M12 are overplotted. Our residuals are a very poor match to these exponential fits: a simple χ^2 test rejects both these fits at over 99% confidence in all cases. Our χ^2 residuals to fits of the exponential profiles found by S11 and M12 are given in Tables 5 and 6, respectively.

The reason for the poor agreement is not solely due to a mismatch in flux: the best-fitting scale lengths for all our putative Lyα halos are relatively small, between 0.″3 and 1.″0 in angular units, or ~3 to ~8 kpc in physical size. This is significantly less (a factor of 2–3) than the 20 to 25 kpc Lyα scale lengths found by S11 in their study of LBGs, and only marginally consistent with the 9–20 kpc scale lengths found in the LAE samples studied by M12. Formally, the derived scale lengths of all

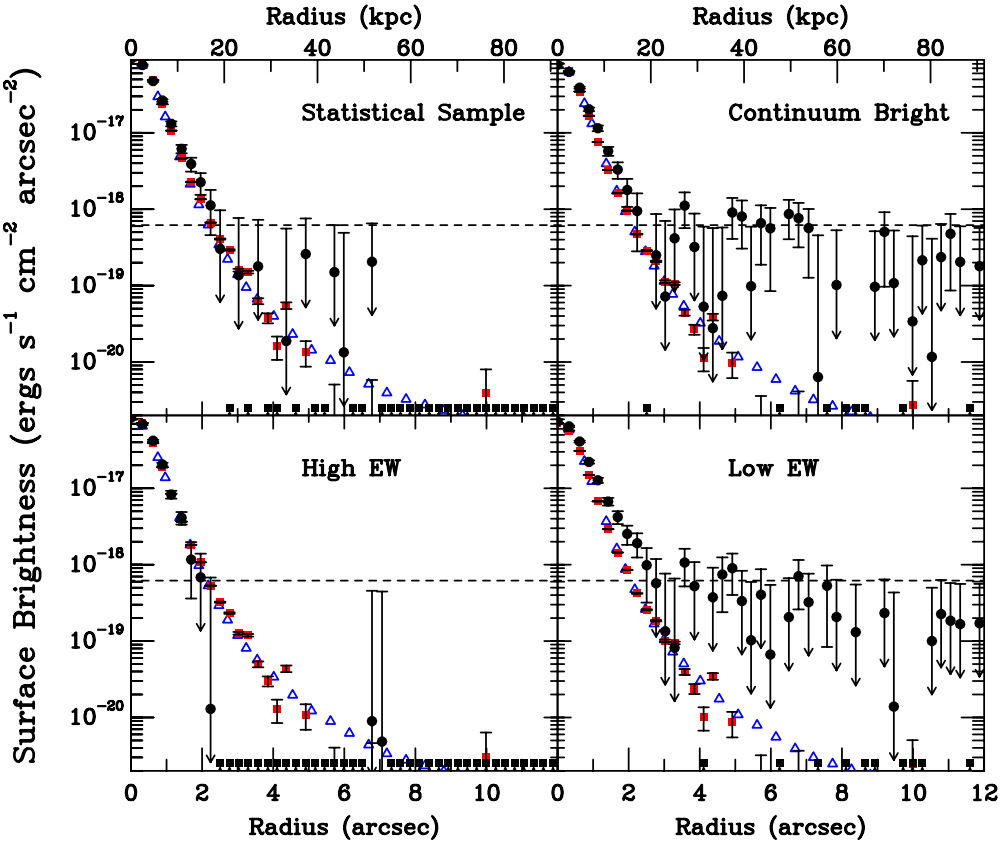

Figure 5. Radial profiles of the LAEs derived from the K-O3 sample, similar to Figure 4.
(A color version of this figure is available in the online journal.)

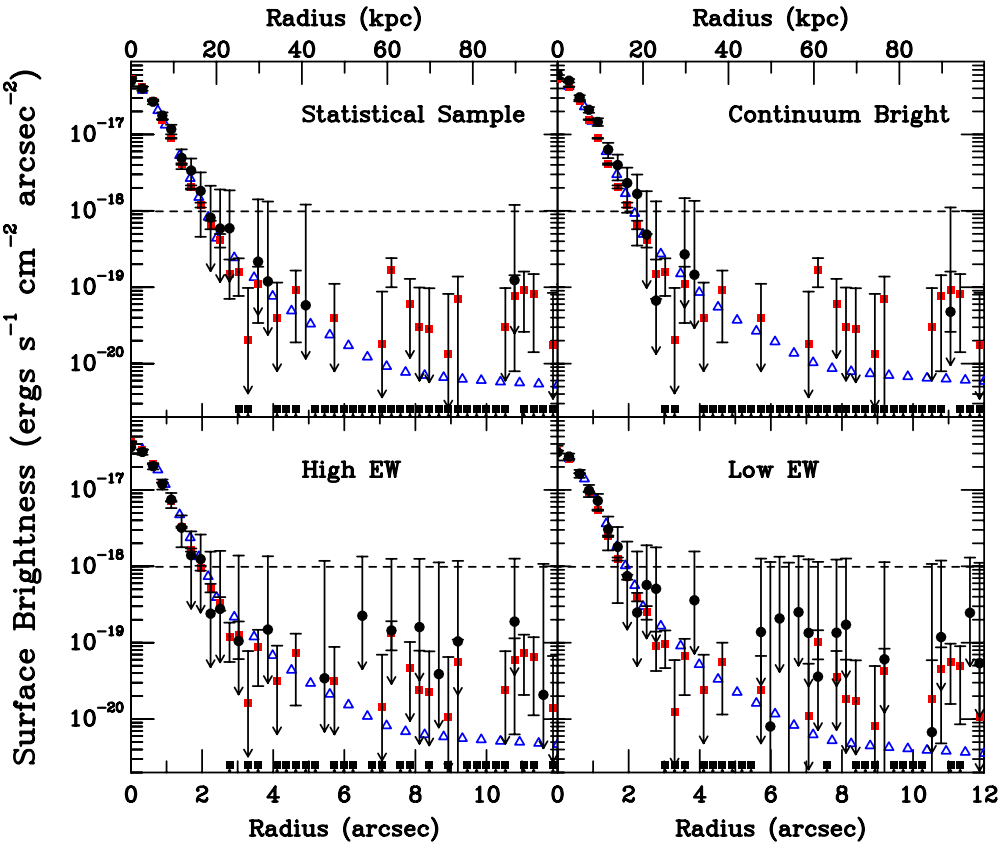

Figure 6. Radial profiles of the LAEs derived from the O2 sample, similar to Figure 4.
(A color version of this figure is available in the online journal.)

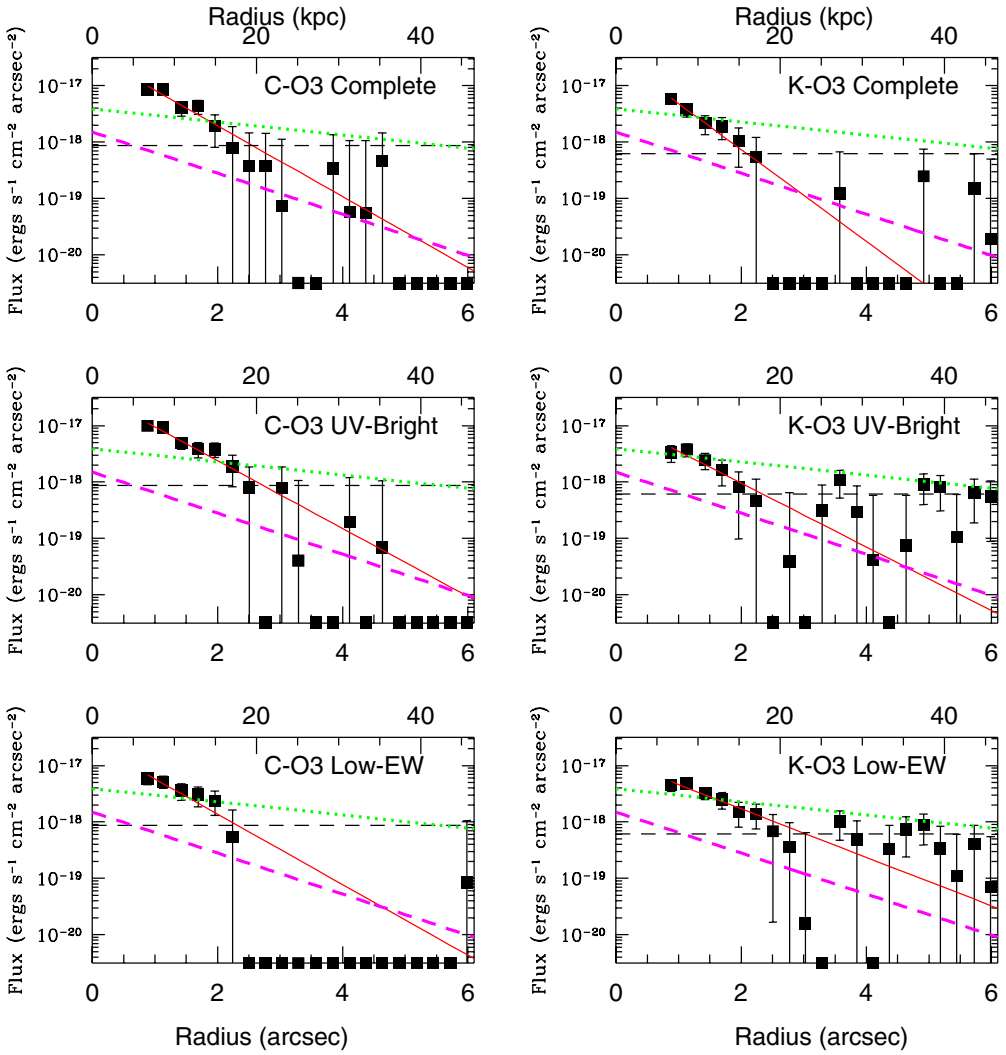

Figure 7. Residual radial profiles of our stacked LAEs, formed by subtracting a scaled version of each frame's point-source stack from the sub-sample's original LAE stack. Sub-samples that display no evidence for extended emission are not shown. Bins with negative flux are denoted by a filled point at the bottom of the plots. The best-fitting exponential model for each sub-sample (given in Table 4) is shown as the solid red line; for comparison purposes, the "LAE only" exponential fit of S11 (see their Table 2) is overplotted as the green dotted line, and the "$-1 < \delta^{a}_{\rm LAE} < 0.5$" (see their Table 1) exponential fit of M12 is overplotted as the dashed magenta line. Both of these fits are poor matches to the data. The horizontal dashed line in each profile represents the limit where systematic uncertainties begin to dominate.

(A color version of this figure is available in the online journal.)

Table 5
Results of χ^2 Tests of Residuals against S11 Exponential Fit

Sample	χ^2	Degrees of Freedom	Reduced χ^2	Null Hypothesis Probability
C-O3 complete	72.54	25	2.90	1.6×10^{-6}
C-O3 UV bright	108.1	25	4.00	2.6×10^{-12}
C-O3 low EW	56.24	25	2.55	1.3×10^{-4}
K-O3 complete	140.4	25	5.62	4.8×10^{-18}
K-03 UV bright	82.67	25	3.31	4.3×10^{-8}
K-O3 low EW	64.49	25	2.59	5.4×10^{-5}

Table 6
Results of χ^2 Tests of Residuals against M12 Exponential Fit

Sample	χ^2	Degrees of Freedom	Reduced χ^2	Null Hypothesis Probability
C-O3 complete	94.54	25	3.78	5.1×10^{-10}
C-O3 UV bright	134.9	25	5.40	4.8×10^{-17}
C-O3 low EW	50.98	25	2.04	1.6×10^{-3}
K-O3 Complete	51.02	25	2.04	1.6×10^{-3}
K-03 UV Bright	49.72	25	1.99	2.3×10^{-3}
K-O3 low EW	74.51	25	2.98	8.1×10^{-7}

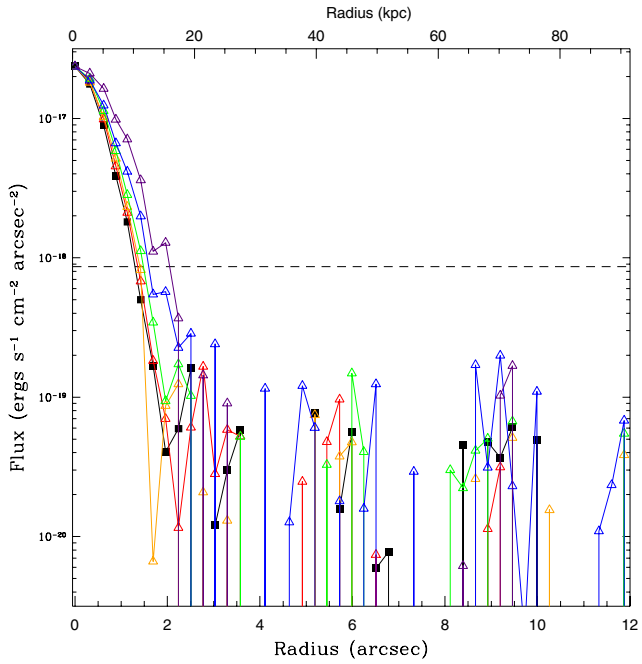

Figure 8. Effects of centroiding errors on our measured profiles. The black filled points represent the co-added profile of 200 artificial point sources (each with a signal-to-noise ratio of 9) on the C-O3 image. The open triangles represent the same data but with differing amounts of $\sigma_{\rm pixel}$, with red, orange, green, blue, and purple (running from closest to furthest away from the solid squares) corresponding to $\sigma_{\rm pixel} = 0.5$, 0.75, 1.0, 1.5, and 2.0 pixels, respectively. Each profile has been normalized to the central point for comparison purposes.

(A color version of this figure is available in the online journal.)

sub-samples are inconsistent with the S11 scale lengths at greater than 99% confidence, and only the K-O3 UV bright and K-O3 low-EW sub-samples are within 2σ of the M12 scale lengths. This result is easily seen in Figure 7, where the best-fitting exponential profiles for our sub-samples are clearly steeper than those of S11 and M12. If the ECDF-S LAEs do have extended Lyα halos, they are much smaller than the halos found by other studies.

Finally, we note that $z \sim 2$ LAEs show no evidence for any LAE halos, as all the profiles displayed in Figure 6 are all consistent with point-source emission. At face value, this is peculiar, since the effects of $(1+z)^4$ cosmological surface brightness dimming should cause $z \sim 3$ halos to be more than $\sim$3 times fainter than their $z \sim 2$ counterparts. The slightly larger angular diameter at $z \sim 2$ also would tend to favor detection of extended emission. While the poorer seeing and slightly brighter sky of the O2 stacks may partly compensate for these effects, the lack of extended emission around the $z \sim 2$ objects may also indicate differences in the populations of LAEs at $z \sim 2$ compared to $z \sim 3$.

5.1. The Effect of Positional Uncertainties

Could some instrumental or sampling issue be affecting our conclusions? Since our analysis is differential in nature, and we are directly comparing the LAEs to point sources using the exact same methods for stacking, averaging, and fitting, it seems unlikely that we are being misled by subtle systematic errors. However, one possible difference between the two samples lies in their mean observed flux. The LAEs measured in Figures 4–6 are, on average, more than 100 times fainter than their point-source counterparts, and hence have larger positional uncertainties. Since the act of stacking relies on knowing the objects' centroids, it is possible that in our co-addition procedure, we have artificially introduced a "halo" into our LAE sample.

Table 7
Effects of Centroiding Errors on Exponential Fits to Point Sources

$\sigma_{\rm pixel}$ (pixels)	C_n[a] (10^{-17} erg s^{-1} cm^{-2} arcsec^{-2})	r_n (arcsec)	r_n[a] (kpc)
0.0	-0.05 ± 0.32	1.3 ± 6.2	11 ± 52
0.5	0.5 ± 4.7	0.4 ± 1.7	3.3 ± 14
0.75	1.1 ± 6.7	0.4 ± 0.9	3.3 ± 7.3
1.0	1.0 ± 3.6	0.5 ± 0.7	4.2 ± 5.8
1.5	0.8 ± 1.7	0.6 ± 0.6	5.0 ± 5.1
2.0	1.2 ± 1.8	0.6 ± 0.4	5.0 ± 3.6

Note. [a] The meaning of these parameters are identical to Table 4.

To quantify the potential strength of this effect we performed a series of Monte-Carlo experiments, each time adding 200 faint (S/N = 9) artificial point sources to the C-O3 frame and stacking the results, while adding a random amount of positional uncertainty, $\sigma_{\rm pixel}$, into the assumed x and y coordinate of each object. Our choice of $\sigma_{\rm pixel}$ spanned the entire range of possible centroiding errors (0.5, 0.75, 1.0, 1.5, and 2.0 pixels), while our flux assignments were chosen to isolate the effects of positioning from that due to the effects of low signal-to-noise ratio. We stacked, averaged, sky subtracted, and fitted these faint artificial point sources in the exact same way as before, and examined the behavior of C_n with $\sigma_{\rm pixel}$. Any non-zero values of C_n would indicate an additional uncertainty above that found from the photometric errors.

As illustrated in Figure 8 and summarized in Table 7, this positional broadening has the potential to mimic the effects of a diffuse halo: large ($\sim$1 pixel) uncertainties in the (x, y) positions of individual LAEs can cause a point-source stacked image to appear extended, and generate a false exponential profile. Obviously, the larger the value of $\sigma_{\rm pixel}$, the larger the size of the apparent halo, so the amplitude of this effect depends strongly on the brightness distribution of the LAE sample being studied.

To determine this quantity, we adopted the LAE flux distribution given in Gronwall et al. (2007), and measured the uncertainty in position as a function of signal-to-noise using a series of artificial star experiments. Our analysis showed that the median coordinate uncertainty for objects near the bright-end of the LAE luminosity function is very small, $\sim$0.05 pixels, while that for objects at the faint end of the statistically complete sample is $\sim$0.5 pixels in the median, and, at worst, $\sim$0.8 pixels. The curves of Figure 8 then suggest that errors in the LAE centroiding can explain some ($\sim$25% of the flux), but not all, of the excesses we detect.

Finally, it is unlikely that the discrepancy between our results and those of S11 and M12 comes from the small differences in the stacking procedures adopted by each study. Our median combination and radial sigma-clipping algorithm has the advantage of being robust against unwanted flux from nearby continuum sources, and is less prone to contamination by unusual objects (such as Lyα blobs) than other methods. Yet the consistent scale lengths found by S11 across all their sub-samples make it unlikely that their result is driven by contamination, and, in any event, their masking procedure should have effectively removed any outlying flux. Similarly, the median stacks computed by M12 should have also been immune against contamination by interlopers. Their method of combining sources without any scaling or object weighting is

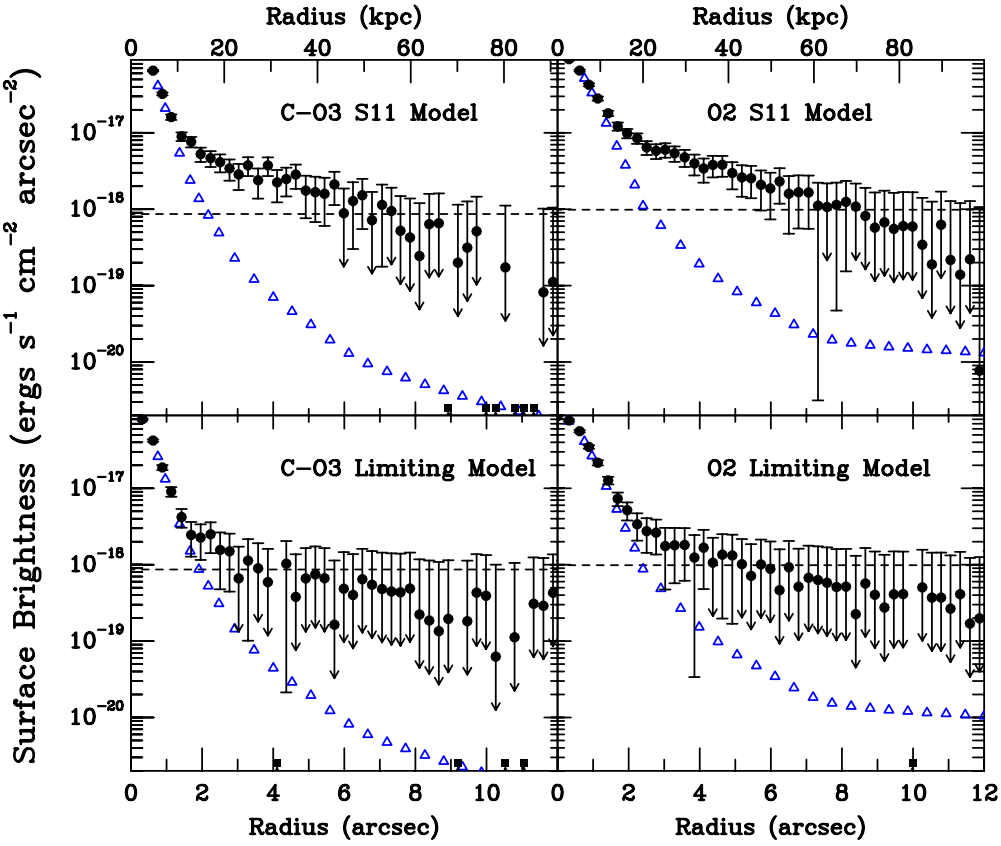

Figure 9. Comparison of Monte-Carlo models with an exponential halo added to the large-scale PSF. The meaning of the symbols is identical to Figure 4. The top row indicates the halo-to-core ratio consistent with the results of S11 ($r_n = 28.4$ kpc). An extended halo of this type would have been clearly detected in our data. The bottom row indicates the models where an extended halo is just barely detected, with a halo-to-core ratio of ≈1.45 in the C-O3 plot, and ≈1.09 in the O2 plot.
(A color version of this figure is available in the online journal.)

slightly sub-optimal in terms of signal-to-noise ratio, but the much larger size of their LAE sample should have overcome this limitation.

We therefore conclude that we have some, but not conclusive, evidence for Lyα halos in our sub-samples. At $z \sim 3$, LAEs with low equivalent widths and bright continuum magnitudes display more evidence for the presence of extended Lyα emission, but due to the uncertainties in flat fielding, sky subtraction, and coordinate centroiding, the detection cannot be considered definitive. Nevertheless, we can say that if Lyα halos do exist in our samples, they are much smaller in physical size than those found by S11 and M12. Moreover, there are clear differences between our results at $z \sim 3$ and $z \sim 2$. Despite the reduced effects of cosmological surface brightness dimming, we see no evidence for any extended halo at the lower redshift.

6. DETERMINING HALO DETECTION LIMITS THROUGH MONTE-CARLO ANALYSIS

Figure 3 and Table 3 illustrate the fundamental limitation of all LAE surface photometry performed over scales greater than ∼100 kpc. It does not address the question of small-scale background fluctuations, and it is at least conceivable that, on galaxy-sized scales, the uniformity of the sky background improves. To test this possibility, we performed a series of Monte-Carlo simulations, using model LAE halos of the form suggested by S11. The goal of these simulations was to ensure that our imaging has sufficient signal-to-noise ratio to detect extended LAE halos, if they are present.

We began by using the GALFIT analysis package (Peng et al. 2002, 2010) to create a set of artificial LAEs, with each LAE consisting of two components: a point-source core, and an exponential halo of the form suggested by S11 (with an adopted scale length, $r_n = 28.4$ kpc). In each simulation, we chose a global halo-to-core flux ratio (corresponding to differing values of C_n), convolved our composite galaxies with the frame's large-scale PSF, and assigned these simulated LAEs random fluxes drawn from the Schechter (1976) luminosity function appropriate for their redshift (Ciardullo et al. 2012). We then randomly placed the artificial galaxies on their respective frames and stacked those objects brighter than the frame's 90% completeness limit. We performed eleven such simulations for the C-O3 and the O2 images, with halo-to-core ratios spaced evenly between zero and four.

The top panels of Figure 9 show the results of these simulations for halos of the type suggested by S11. It is clear that at this halo-to-core ratio (corresponding to $C_n \approx 4.6 \times 10^{-18}$ erg cm^{-2} s^{-1} arcsec^{-2} for the C-O3 stacks, and $C_n \approx 1.1 \times 10^{-17}$ erg cm^{-2} s^{-1} arcsec^{-2} for the O2 stacks), extended Lyα emission would have been easily detected, and their morphology would have been quite different from the observed profiles displayed in Figures 4–7. The panels also demonstrate that the surface brightness limits to which we can confidently trace Lyα emission are similar to those predicted by the large-scale flat-fielding error. Even at scales less than ∼100 kpc, the

systematic effects discussed in Section 4 are still the dominant error terms in our analysis.

Of course, it is certainly possible that the Lyα halos of high-redshift LAEs are fainter than those described by S11, and have correspondingly smaller values of C_n. To examine this possibility, we visually inspected and repeated our non-linear least squares analysis on simulated halos with smaller halo-to-core ratios. The bottom panels of Figure 9 illustrate those models with marginally detected halos. In the C-O3 panel, we found a limiting value of $C_n \approx 2 \times 10^{-18}$ erg cm^{-2} s^{-1} arcsec^{-2}, while in the O2 plot, the limiting value of C_n is $\approx 4 \times 10^{-18}$ erg cm^{-2} s^{-1} arcsec^{-2} Any LAE halos with fluxes below these limits would be undetectable on our images. We note that the stacked Lyα halo found by S11 for LBGs is relatively bright, as it contains $\sim$3.4 times more flux than the galaxy's central core. The halos detected by M12, however, are substantially fainter, with best fit values for C_n ranging from 3.2 down to 0.7×10^{-18} erg cm^{-2} s^{-1} arcsec^{-2}. Therefore, in our LAE samples, the relatively bright halos suggested by S11 are ruled out, while the fainter halos claimed by M12 may still exist.

7. DISCUSSION

Most cosmological simulations—even those that include radiative transfer from Lyα—do not include the effects of resonant scattering of photons from the inter- and circumgalactic medium. One exception is the work of Zheng et al. (2011), who calculated the expected spatial distribution of extended Lyα emission from LAEs at $z \sim 6$. These models predict that in the Lyα emission line, a high-redshift LAE should have a central cusp, and a slowly declining envelope which extends outward from $\sim$0.2 Mpc to $\sim$1 Mpc (in co-moving distance). Unfortunately, it is difficult to directly compare our observational results at $2 < z < 3$ to the predictions of these models. The distribution of gas at $z \sim 6$ is largely defined by infall, and is related to the virial radius of the galaxy; both these parameters evolve rapidly in the Gyr between $z \sim 6$ and $z \sim 3$. In addition, the Zheng et al. (2011) models have a poorer spatial resolution than our data, making it difficult to compare except at the largest radii. These simulations also do not include the effects of dust, and, depending on how this component is distributed, its effect on the propagation of Lyα photons can be dramatic (e.g., Neufeld 1991; Finkelstein et al. 2009b). Finally, the Zheng et al. (2011) models do not take into account the internal structure and kinematics of the ISM. Thus, it is not possible to directly compare their model predictions with observational results.

More recently, Dijkstra & Kramer (2012) performed radiative transfer calculations for Lyα photons propagating through clumpy, dusty, large-scale outflows. While these authors do predict the existence of extended Lyα halos, their initial models (I–III) have halos that are more concentrated (inner scale lengths of $\sim$4 kpc) than those observed by S11, and are fainter by almost an order of magnitude ($\approx 4.5 \times 10^{-20}$ erg cm^{-2} s^{-1} arcsec^{-2} at a radius of $\approx 5''$). More complex models (IV–V) that include the deceleration of clumps are better matches to the halos observed by S11, but still underpredict the flux by a factor of two to three. Unfortunately, due to our observational limits, we would not be able to detect halos of these types; only the two innermost points of their halos would be measurable in our data, with fluxes of $0.1\text{–}1 \times 10^{-17}$ erg cm^{-2} s^{-1} arcsec^{-2}. Several recent studies of Lyα emitters within a cosmological framework explicitly include explicit radiative transfer, and these could be applied to the problem of Lyα halos (Forero-Romero et al. 2011; Garel et al. 2012; Orsi et al. 2012).

As detailed above, accurate surface photometry at low flux levels is difficult, and fraught with systematic errors. Consequently, direct comparisons with other Lyα halo measurements is difficult and may ignore important systematic effects. Using long-slit spectroscopy, Rauch et al. (2008) found extended Lyα emission in roughly half of a sample of 27 LAEs in the redshift range $2.7 \leqslant z \leqslant 3.8$. But this emission was weak: no brighter than $\sim 1.8 \times 10^{-19}$ erg s^{-1} cm^{-2} arcsec^{-2} at $\sim 4''$ ($\sim$30 kpc) and well below the level where systematic uncertainties dominate our error budget. Yet a similar study by Cassata et al. (2011) on 217 LAEs in the redshift range $2 \leqslant z \leqslant 6.6$ found no evidence for extended Lyα, as all their objects were found to be compact (FWHM $\sim 0\farcs9$). M12, by using the stacked images of several hundred field LAEs found on Subaru frames, found halos at the level of 1×10^{-18} erg s^{-1} cm^{-2} arcsec^{-2}. For comparison, the LBG halos of S11 and Hayashino et al. (2004), which were measured in highly overdense regions of the universe, are almost an order of magnitude brighter. Other attempts to image LAE halos, both from the ground (Smith et al. 2012), and from space (Bond et al. 2010; Finkelstein et al. 2011b) have placed only weak upper limits on the phenomenon, and generally probe very different spatial scales. Recently, Jiang et al. (2013) has stacked LAEs at $z \simeq 5.7$ and 6.5 and has not found signs of extended LAE halos.

S11 hypothesize that extended Lyα halos are a "generic property of high-redshift star-forming galaxies," while M12 argue that the emission properties of Lyα halos depend on environment. Neither of these studies took into account the systematics associated with the large radius PSF or large-scale flat fielding, but neither are in direct conflict with our results. The median LAE in our analysis is over a magnitude fainter than the LBGs studied by S11, and our surface brightness limits, 9.9×10^{-19} erg s^{-1} cm^{-2} arcsec^{-2} for $z \sim 2.1$ and 8.7×10^{-19} and 6.2×10^{-19} erg s^{-1} cm^{-2} arcsec^{-2} for the two $z \sim 3.1$ samples are brighter than the values quoted by M12. Thus, there are several ways to reconcile the three surveys.

First, LAEs may have significantly fainter Lyα halos than LBGs. In general, the SFRs of LAEs are an order of magnitude smaller than those of LBGs (e.g., Gronwall et al. 2007), and it is reasonable to hypothesize that the lower masses associated with LAEs also imply less circumgalactic material. These two factors may combine to produce Lyα halos whose surface brightness is highly sensitive to the luminosity of the underlying galaxy. This argument is somewhat mitigated by the fact that LBGs have more internal extinction than their LAE counterparts, but there are ways to distribute this dust so that the resonantly scattered Lyα photons can escape their surroundings (Neufeld 1991; Finkelstein et al. 2009b). The fact that our best evidence for extended emission occurs on the C-O3 and K-O3 stacks of LBG-like objects and low-equivalent width sources argues in support of this interpretation.

Alternatively, the observability of Lyα halos may be largely due to galactic geometry. The probability of detecting Lyα emission from a galaxy depends on many factors, including viewing angle, dust content, gas dynamics, and intrinsic geometry. By definition, LAEs are systems where the Lyα escape path falls along our line-of-sight; in galaxies selected via the Lyman-break technique, Lyα may leak out in other directions, thus facilitating the detection of a "halo." S11's data argue against this interpretation, since the halos surrounding LBGs with Lyα emission are no different from those where Lyα was only seen in absorption. However, the Lyα equivalent widths of typical LAEs are much greater than those associated with LBGs, so this selection effect

may still play a role. Recently, Verhamme et al. (2012) have claimed that Lyα emission from galaxies can have strong inclination effects, with LAEs with high equivalent widths being more likely to be found in face-on, rather than edge-on orientations. Although there are many details still left to be resolved, it is also worth noting that the simulations of Verhamme et al. (2012) show a substantially weaker halo than S11.

A third possibility concerns environment. M12 have argued that a galaxy's surroundings play an important role in the observability of Lyα emission. The LBGs studied by S11 are primarily located in overdense regions of the universe, including the well-known field SSA22 (Steidel et al. 1998) and two regions centered on hyper-luminous QSOs (HS1700+64 and HS1549+195). In these "proto-cluster" environments, there is likely to be a large amount of circumgalactic material, which could scatter the Lyα photons which escape from galaxies. Indeed, not only is SSA22 known for possessing large numbers of luminous Lyα blobs (e.g., Matsuda et al. 2004; Steidel et al. 2000), but, according to M12, its LAEs are similar in strength and profile to those found by S11 for the region's LBGs. In lower density regions, M12 found the Lyα halos of LAEs to have steeper profiles with less total luminosity. The LAEs studied in this paper are all in the blank-field environment of the ECDF-S, which is equivalent to the $-1 < \delta^{a}_{\rm LAE} < 0.5$ sub-sample of M12. If this is true, then the lack of halo emission around our galaxies should not be too surprising.

Finally, we note that our Lyα halo measurements at $z \sim 3.1$ differ from those at $z \sim 2.1$: despite the $(1+z)^4$ gain in surface brightness, we see no evidence for extended Lyα halos in any of our lower-redshift sub-samples. One possible explanation for this difference lies in the uniformity of LAE populations. A number of analyses have shown that LAEs at $z \sim 2.1$ are, on average, slightly larger, dustier, and more heterogeneous than their $z \sim 3.1$ counterparts (Nilsson et al. 2009, 2011; Guaita et al. 2011; Bond et al. 2012). It is possible that this diversity at lower redshift might also lead to differences in halo properties.

8. CONCLUSION

Surface photometry at very low flux levels is treacherous, and extreme care must be used in modeling systematics such as the large-radius PSF and the large-scale flat-fielding errors. By taking such factors into account, we were able to form stacked profiles of three sets of LAEs in the Lyα emission-line and to obtain robust estimates of their uncertainties. At $z \sim 3.1$, we find mixed evidence for the presence of extended Lyα halos down to a surface brightness limit of $\approx 7 \times 10^{-19}$ erg cm^{-2} s^{-1} arcsec^{-2}. At $z \sim 2.1$, where cosmological dimming is a factor of 3.2 less, we see no extended emission down to surface brightnesses of $\approx 1 \times 10^{-18}$ erg cm^{-2} s^{-1} arcsec^{-2}. This is the first time the rigorous techniques of low flux level surface photometry have been applied to the problem of galactic emission-line halos.

While our observations are not in direct conflict with those of Steidel et al. (2011) and Matsuda et al. (2012), they do place important constraints on the systematic behavior of Lyα halos and imply that such studies have higher uncertainties than originally thought. However, further progress on this problem will be difficult in the near-term. To successfully image the emission-line halos around LAE and LBG halos, one should obtain deep narrow-band exposures on telescopes with WFIs that also have low scattered light profiles and very stable flat-fields. This means paying close attention to the details of baffling and flat-fielding (i.e., taking the dark-sky flat flat-fields at the same hour angle as the observations) and using closed-tube telescopes with cameras designed to minimize the total number of internal reflections. Our observations, as well as those of S11 and M12, were performed with open-tube telescopes and WFIs that contained multi-component optical corrector systems. As this is the norm for large wide-field imaging telescopes, it will be difficult to extend imaging surveys much below the surface brightness limits achieved here, though observations of additional fields will allow for better determination of systematic effects and allow us to better probe the effects of galactic environment on LAE halos.

Alternatively, it is possible to study the emission-line halos of high-redshift galaxies with spectroscopy. Starting in 2014, the integral-field units of the Hobby–Eberly Telescope Dark Energy Experiment (HETDEX) will obtain two-dimensional spectra for $\sim 10^6$ Lyα emitters in the redshift range $1.9 < z < 3.5$ (Hill et al. 2007). These data, which will have $\sim 0\farcs5$ spatial resolution and ~ 6 Å spectral resolution, should allow us to trace circumgalactic Lyα emission to levels far below what is currently possible and to determine the properties of these systems as a function of luminosity, equivalent width, dust content, redshift, and environment, and thus illuminate material in the high-redshift universe's cosmic web.

This work was supported by NSF grants AST 06-07416, AST 08-07570, AST 08-07873, AST 08-07885, and AST 10-55919, and DOE grants DE-GF02-08ER41560 and DE-FG02-08ER41561. The Institute for Gravitation and the Cosmos is supported by the Eberly College of Science and the Office of the Senior Vice President for Research at the Pennsylvania State University.

We acknowledge valuable discussions with Lennox Cowie, Esther Hu, Sangeeta Malhotra, James Rhoads, and Tomoki Saito. We also thank the anonymous referee for several suggestions that improved the quality of this paper. We thank the staff of Cerro Tololo Inter-American Observatory for their assistance with our observations. This research has made use of NASA's Astrophysics Data System.

Facility: Blanco (MOSAIC II)

REFERENCES

Acquaviva, V., Gawiser, E., & Guaita, L. 2011, ApJ, 737, 47
Adams, J. J., Blanc, G. A., Hill, G. J., et al. 2011, ApJS, 192, 5
Adelberger, K. L., Steidel, C. C., Pettini, M., et al. 2005, ApJ, 619, 697
Adelberger, K. L., Steidel, C. C., Shapley, A. E., & Pettini, M. 2003, ApJ, 584, 45
Altmann, M., Méndez, R. A., van Altena, W., Korchargin, V., & Ruiz, M. T. 2006, RMxAA, 26, 64
Barger, A. J., Cowie, L. L., & Wold, I. G. B. 2012, ApJ, 749, 106
Barnes, L. A., Haehnelt, M. G., Tescari, E., & Viel, M. 2011, MNRAS, 416, 1723
Bernstein, R. A. 2007, ApJ, 666, 663
Berry, M., Gawiser, E., Guaita, L., et al. 2012, ApJ, 749, 4
Bertin, E., & Arnouts, S. 1996, A&AS, 117, 393
Blanc, G. A., Adams, J. J., Gebhardt, K., et al. 2011, ApJ, 736, 31
Bond, N. A., Feldmeier, J. J., Matković, A., et al. 2010, ApJL, 716, L200
Bond, N. A., Gawiser, E., Guaita, L., et al. 2012, ApJ, 753, 95
Bond, N. A., Gawiser, E., & Koekemoer, A. M. 2011, ApJ, 729, 48
Cassata, P., Le Fèvre, O., Garilli, B., et al. 2011, A&A, 525, A143
Ciardullo, R., Gronwall, C., Wolf, C., et al. 2012, ApJ, 744, 110
Cowie, L. L., Barger, A. J., & Hu, E. M. 2011, ApJ, 738, 136
Davé, R., Finlator, K., & Oppenheimer, B. D. 2011a, MNRAS, 416, 1354
Davé, R., Oppenheimer, B. D., & Finlator, K. 2011b, MNRAS, 415, 11
Dekel, A., Sari, R., & Ceverino, D. 2009, ApJ, 703, 785
Dijkstra, M., & Kramer, R. 2012, MNRAS, 424, 1672
Feldmeier, J. J., Mihos, J. C., Morrison, H. L., Rodney, S. A., & Harding, P. 2002, ApJ, 575, 779
Feldmeier, J. J., Mihos, J. C., Morrison, H. L., et al. 2004, ApJ, 609, 617

Finkelstein, S. L., Cohen, S. H., Malhotra, S., & Rhoads, J. E. 2009a, ApJ, 700, 276
Finkelstein, S. L., Cohen, S. H., Moustakas, J., et al. 2011a, ApJ, 733, 117
Finkelstein, S. L., Cohen, S. H., Windhorst, R. A., et al. 2011b, ApJ, 735, 5
Finkelstein, S. L., Hill, G. J., Gebhardt, K., et al. 2011c, ApJ, 729, 140
Finkelstein, S. L., Papovich, C., Giavalisco, M., et al. 2010, ApJ, 719, 1250
Finkelstein, S. L., Rhoads, J. E., Malhotra, S., & Grogin, N. 2009b, ApJ, 691, 465
Forero-Romero, J. E., Yepes, G., Gottlöber, S., et al. 2011, MNRAS, 415, 3666
Francke, H. 2009, NewAR, 53, 47
Garel, T., Blaizot, J., Guiderdoni, B., et al. 2012, MNRAS, 422, 310
Gawiser, E., Francke, H., Lai, K., et al. 2007, ApJ, 671, 278
Gawiser, E., van Dokkum, P. G., Gronwall, C., et al. 2006a, ApJL, 642, L13
Gawiser, E., van Dokkum, P. G., Herrera, D., et al. 2006b, ApJS, 162, 1
Gonzalez, A. H., Zabludoff, A. I., & Zaritsky, D. 2005, ApJ, 618, 195
Gonzalez, A. H., Zabludoff, A. I., Zaritsky, D., & Dalcanton, J. J. 2000, ApJ, 536, 561
Gronwall, C., Ciardullo, R., Hickey, T., et al. 2007, ApJ, 667, 79
Grundahl, F., & Sorensen, A. N. 1996, A&AS, 116, 367
Guaita, L., Acquaviva, V., Padilla, N., et al. 2011, ApJ, 733, 114
Guaita, L., Gawiser, E., Padilla, N., et al. 2010, ApJ, 714, 255
Hashimoto, T., Ouchi, M., Shimasaku, K., et al. 2013, ApJ, 765, 70
Hayashino, T., Matsuda, Y., Tamura, H., et al. 2004, AJ, 128, 2073
Hibon, P., Cuby, J.-G., Willis, J., et al. 2010, A&A, 515, A97
Hildebrandt, H., Erben, T., Dietrich, J. P., et al. 2006, A&A, 452, 1121
Hill, G. J., Gebhardt, K., Komatsu, E., et al. 2007, in ASP Conf. Ser. 399, Panoramic Views of Galaxy Formation and Evolution, ed. T. Kodama, T. Yamada, & K. Aoki (San Francisco, CA: ASP), 115
Hoversten, E. A., Gronwall, C., Vanden Berk, D. E., et al. 2009, ApJ, 705, 1462
Hu, E. M., Cowie, L. L., Barger, A. J., et al. 2010, ApJ, 725, 394
Jiang, L., Egami, E., Fan, X., et al. 2013, ApJ, 773, 153
King, I. R. 1971, PASP, 83, 199
Krick, J. E., Bernstein, R. A., & Pimbblet, K. A. 2006, AJ, 131, 168
Krug, H. B., Veilleux, S., Tilvi, V., et al. 2012, ApJ, 745, 122
Kulas, K. R., Shapley, A. E., Kollmeier, J. A., et al. 2012, ApJ, 745, 33
Labbé, I., González, V., Bouwens, R. J., et al. 2010, ApJL, 716, L103
Lai, K., Huang, J.-S., Fazio, G., et al. 2008, ApJ, 674, 70
Laursen, P., Sommer-Larsen, J., & Andersen, A. C. 2009, ApJ, 704, 1640
Lehmer, B. D., Brandt, W. N., Alexander, D. M., et al. 2005, ApJS, 161, 21
Luo, B., Bauer, F. E., Brandt, W. N., et al. 2008, ApJS, 179, 19
Malhotra, S., Rhoads, J. E., Finkelstein, S. L., et al. 2012, ApJL, 750, L36
Mallery, R. P., Mobasher, B., Capak, P., et al. 2012, ApJ, 760, 128
Martínez-Delgado, D., Peñarrubia, J., Gabany, R. J., et al. 2008, ApJ, 689, 184
Matsuda, Y., Yamada, T., Hayashino, T., et al. 2004, AJ, 128, 569
Matsuda, Y., Yamada, T., Hayashino, T., et al. 2012, MNRAS, 425, 878
McLinden, E. M., Finkelstein, S. L., Rhoads, J. E., et al. 2011, ApJ, 730, 136
Melnick, J., Selman, F., & Quintana, H. 1999, PASP, 111, 1444
Morrison, H. L., Boroson, T. A., & Harding, P. 1994, AJ, 108, 1191
Muller, G. P., Reed, R., Armandroff, T., Boroson, T. A., & Jacoby, G. H. 1998, Proc. SPIE, 3355, 577
Nakajima, K., Ouchi, M., Shimasaku, K., et al. 2012, ApJ, 745, 12
Neufeld, D. A. 1991, ApJL, 370, L85
Nilsson, K. K., Møller, P., Möller, O., et al. 2007, A&A, 471, 71
Nilsson, K. K., Östlin, G., Møller, P., et al. 2011, A&A, 529, A9
Nilsson, K. K., Tapken, C., Møller, P., et al. 2009, A&A, 498, 13
Ono, Y., Ouchi, M., Shimasaku, K., et al. 2010, MNRAS, 402, 1580
Orsi, A., Lacey, C. G., & Baugh, C. M. 2012, MNRAS, 425, 87
Östlin, G., Hayes, M., Kunth, D., et al. 2009, AJ, 138, 923
Ota, K., Iye, M., Kashikawa, N., et al. 2010, ApJ, 722, 803
Oteo, I., Bongiovanni, A., Pérez García, A. M., et al. 2012, ApJ, 751, 139
Ouchi, M., Shimasaku, K., Akiyama, M., et al. 2008, ApJS, 176, 301
Ouchi, M., Shimasaku, K., Furusawa, H., et al. 2010, ApJ, 723, 869
Paudel, S., Duc, P.-A., Côté, P., et al. 2013, ApJ, 767, 133
Peng, C. Y., Ho, L. C., Impey, C. D., & Rix, H. 2002, AJ, 124, 266
Peng, C. Y., Ho, L. C., Impey, C. D., & Rix, H.-W. 2010, AJ, 139, 2097
Pirzkal, N., Malhotra, S., Rhoads, J. E., & Xu, C. 2007, ApJ, 667, 49
Prescott, M. K. M., Dey, A., & Jannuzi, B. T. 2012, ApJ, 748, 125
Press, W. H., Teukolsky, S. A., Vetterling, W. T., & Flannery, B. P. 1992, Numerical Recipes in Fortran – The Art of Scientific Computing (2nd ed.; Cambridge: Cambridge Univ. Press)
Rauch, M., Haehnelt, M., Bunker, A., et al. 2008, ApJ, 681, 856
Rudick, C. S., Mihos, J. C., Harding, P., et al. 2010, ApJ, 720, 569
Saito, T., Shimasaku, K., Okamura, S., et al. 2006, ApJ, 648, 54
Salvadori, S., Dayal, P., & Ferrara, A. 2010, MNRAS, 407, L1
Schechter, P. 1976, ApJ, 203, 297
Schiminovich, D., Arnouts, S., Milliard, B., & GALEX Science Team. 2003, BAAS, 35, 1371
Shapley, A. E., Steidel, C. C., Adelberger, K. L., et al. 2001, ApJ, 562, 95
Shapley, A. E., Steidel, C. C., Pettini, M., & Adelberger, K. L. 2003, ApJ, 588, 65
Slater, C. T., Harding, P., & Mihos, J. C. 2009, PASP, 121, 1267
Smith, B. M., Malhotra, S., Rhoads, J., et al. 2012, BAAS, 219, 340.06
Stark, D. P., Ellis, R. S., Bunker, A., et al. 2009, ApJ, 697, 1493
Steidel, C. C., Adelberger, K. L., Dickinson, M., et al. 1998, ApJ, 492, 428
Steidel, C. C., Adelberger, K. L., Shapley, A. E., et al. 2000, ApJ, 532, 170
Steidel, C. C., Bogosavljević, M., Shapley, A. E., et al. 2011, ApJ, 736, 160 (S11)
Steidel, C. C., Erb, D. K., Shapley, A. E., et al. 2010, ApJ, 717, 289
Steidel, C. C., Giavalisco, M., Pettini, M., Dickinson, M., & Adelberger, K. L. 1996, ApJL, 462, L17
Stetson, P. B. 1987, PASP, 99, 191
Tapken, C., Appenzeller, I., Noll, S., et al. 2007, A&A, 467, 63
Tilvi, V., Rhoads, J. E., Hibon, P., et al. 2010, ApJ, 721, 1853
Veilleux, S., Cecil, G., & Bland-Hawthorn, J. 2005, ARA&A, 43, 769
Verhamme, A., Dubois, Y., Blaizot, J., et al. 2012, A&A, 546, A111
Verhamme, A., Schaerer, D., Atek, H., & Tapken, C. 2008, A&A, 491, 89
Verhamme, A., Schaerer, D., & Maselli, A. 2006, A&A, 460, 397
Virani, S. N., Treister, E., Urry, C. M., & Gawiser, E. 2006, AJ, 131, 2373
Wang, J.-X., Malhotra, S., Rhoads, J. E., Zhang, H.-T., & Finkelstein, S. L. 2009, ApJ, 706, 762
Windhorst, R. A., Cohen, S. H., Hathi, N. P., et al. 2011, ApJS, 193, 27
Yajima, H., Li, Y., Zhu, Q., et al. 2012, ApJ, 754, 118
Yuma, S., Ohta, K., Yabe, K., et al. 2010, ApJ, 720, 1016
Zheng, Z., Cen, R., Weinberg, D., Trac, H., & Miralda-Escudé, J. 2011, ApJ, 739, 62
Zheng, Z., Shang, Z., Su, H., et al. 1999, AJ, 117, 2757
Zibetti, S., White, S. D. M., Schneider, D. P., & Brinkmann, J. 2005, MNRAS, 358, 949